Ballistic photocurrent driven by optical phonon modes in a polaronic ferroelectric

Sangeeta Rajpurohit,[1,*] Tadashi Ogitsu,[2] and Liang Z. Tan[1]
[1]*Molecular Foundry, Lawrence Berkeley National Laboratory, Berkeley, California 94720, USA*
[2]*Lawrence Livermore National Laboratory, Livermore, California 94550, USA*

(Received 17 August 2022; revised 20 March 2023; accepted 19 July 2023; published 6 September 2023)

We investigate the effect of local electron-phonon coupling on nonlinear optical conductivity in an interacting ferroelectric system. Using real-time simulations, we show an enhancement in nonlinear conductivity under linearly polarized light due to generation of the phonon-assisted ballistic current in addition to the injection current generated by electron-hole pairs. The optically excited phonon modes generate an asymmetric carrier distribution that causes a strong directional ballistic current. The ballistic current enhances the photocurrent several times at above band-gap excitation frequencies and is sublinearly dependent on the excitation intensity. This strong phonon-assisted zero-frequency directional ballistic current demonstrates an alternative way to boost the bulk photovoltaic effect (BPVE) in electronic ferroelectric materials with strong local electron-phonon coupling.

DOI: 10.1103/PhysRevB.108.104305

I. INTRODUCTION

The nonlinear optical effects in quantum materials have been extensively studied due to their strong fundamental and technological relevance [1,2]. For example, the coupling between the polarization and optical properties in solids lacking inversion symmetry, such as ferroelectrics, causes unconventional photovoltaic effects, known as bulk photovoltaic effect (BPVE) [3,4]. The BPVE is the generation of directional (dc) photocurrent due to above-bandgap electronic excitations under an external electric field [3,5].

The dc current generated in BPVE can be classified into two types: shift current and ballistic current [6–8]. The shift current is a purely coherent quantum phenomenon that involves the relative shift of the electron cloud in real space during excitation under linearly polarized light. It is independent of any scattering mechanism, and its relaxation occurs at electronic timescales. On the other hand, the ballistic current (also referred to as injection current) arises from the asymmetric momentum distribution of carriers due to scattering processes such as electron-phonon (el-ph) [4,6,9–12], electron-electron (el-el) [13], and electron-spin (el-s) scattering. Another form of injection current is present under circularly polarized light, where population asymmetry is generated by photoexcitation instead of scattering [14]. Higher-order photocurrents which involve population asymmetry depend on various kinetic processes that span a range of time scales [15,16], unlike the coherent shift current process.

While past theoretical studies of the BPVE have mostly been performed in perturbation theory, recent works have shown that naive application of perturbation theory can lead to incorrect results for the shift and injection currents in certain limits [17]. Furthermore, the use of the independent-particle approximation in the frozen band picture limits the predictive power of such studies in nonperturbation regions [13]. Dynamical effects, such as carrier momentum and energy relaxation due to elastic and inelastic scattering, are known to significantly affect the BPVE properties of materials [13,17–19]. The rate of relaxation of energy and momentum depends on the interactions el-ph, el-el, and el-s and impurities, all of which are intrinsic properties of materials [20,21]. In addition to carrier scattering, quasiparticle effects, such as excitonic dynamics, are also known to affect photocurrent dynamics and produce a nontrivial photovoltaic response [13,17–19].

The phonon-induced ballistic current has only been treated within perturbation theory in previous studies [9,22]. With the limitations of perturbation theory for shift and injection currents in mind, we re-examine the phonon-induced ballistic current using nonpertubative real-time simulations in the present study. We demonstrate that a phonon-induced ballistic current can be sustained at steady state, using a one-dimensional (1D) polaronic ferroelectric system as an illustrative model. Importantly, optical phonon modes coupled to charge-transfer electronic excitations causing strong asymmetric el-ph scattering are necessary for generating a strong ballistic photocurrent. We show that this is possible through a Holstein-type coupling to optical phonon modes. This phonon-assisted current is unidirectional, and results in a strong BPVE response independent of light polarization. The magnitude of the reported ballistic current originating from optical phonon modes is the largest contributor to the BPVE in this system. We observe a departure from the predictions perturbation theory in the high intensity limit. Our reported large contribution of the ballistic-current to BPVE originating from phonon dynamics can explain the temperature dependence of the photocurrent, which cannot be resolved by the shift current theory, recently observed in the ferroelectric organic molecular system [23].

*srajpurohit@lbl.gov

Our study suggests possibilities for strengthening the nonlinear optical rectification and the BPVE effect in ferroelectrics with strong el-ph interactions displaying bound excitations and long-lived optically excited high-frequency phonon modes, such as complex transition-metal oxides or charge-transfer organic salts.

This paper is structured as follows. The one-dimensional ferroelectric model is introduced and described in Sec. II. In Sec. III, we report the strong phonon-assisted BPVE effect in the polaronic ferroelectric phase. We discuss the current versus intensity behavior, its spectral distribution, and the effect of model parameters on the photocurrent. Finally, we summarize the main findings of our work in Sec. IV.

II. ONE-DIMENSIONAL FERROELECTRIC MODEL

We consider a minimal one-dimensional ferroelectric model [24] with an el-ph interaction. Motivated by three-dimensional ABO_3 transition-metal perovskite oxides, the model consists of a chain of corner-connected BO_6-octahedra with the z axis along the chain. The Hilbert space consists of a single electron orbital on each B-type ion. Electronic hopping between these B-type orbitals is mediated via intermediate O-type sites, similar to transition-metal oxides. The electrons are described by a Slater determinant formed by the one-particle wavefunctions $|\psi_n\rangle$. Each wave function $|\psi_n\rangle$ is a two-component spinor and is expressed as $|\psi_n\rangle = \sum_j |\chi_{\sigma,j}\rangle\psi_{\sigma,j,n}$, with band index n and occupation f_n in terms of local spin-orbital $|\chi_{\sigma,j}\rangle$ at every jth B-type site. The potential energy $E_{\rm pot}(|\psi_n\rangle, Q_j)$ in this interacting ferroelectric model is defined as

$$\begin{aligned} E_{\rm pot} = &\sum_n f_n \sum_{j,\sigma} (t_{\rm hop} + (-1)^j\delta)(\psi_{\sigma,j,n}\psi^*_{\sigma,j+1,n} \\ &+ \psi_{\sigma,j+1,n}\psi^*_{\sigma,j,n}) - g_{br}\sum_{j,\sigma}\rho_{\sigma,\sigma,j}Q_j + K/2\sum_j Q_j^2 \\ &+ U/2\sum_{j,\sigma\neq\sigma'}(\rho_{\sigma,\sigma,j}\rho_{\sigma',\sigma',j} - \rho_{\sigma,\sigma',j}\rho_{\sigma',\sigma,j}). \end{aligned} \quad (1)$$

The first and second terms correspond to the electron hopping between B-sites and the el-ph interaction, respectively. $t_{\rm hop}$ and g_{br} are the strengths of the hopping and el-ph coupling. For every jth B-site, we consider the local octahedral breathing mode Q_j, defined as $Q_j = 1/\sqrt{(}3)(d_{x,i} + d_{y,i} + d_{z,i} - 3\bar{d})$ where $d_{x/y/z,i}$ is the distance between O-type ions forming octahedra around the ith B-site along $x/y/z$ direction and $\bar{d} = 3.85$ Å is the equilibrium O-O distance. These Q_j modes are coupled to the electron density at the respective jth B-sites. The third term in $E_{\rm pot}$ is the potential energy of the displacements of u_i, where K is the restoring force constant.

The restoring force constant K is related to the mass M_O and the vibration frequency of the phonon mode Q_i by $K = M_O\omega_b^2$. We fix $K = 10$ eV/Å^2 so that the vibration frequency of the Q_j modes, assuming M_O as the mass of oxygen atoms, is in the range of the frequencies of optical phonon modes such as Jahn-Teller and breathing modes, in transition-metal oxides.

Finally, we include local el-el interactions via the U parameter. This term incorporates a fast decoherence and relaxation effect within the electronic subsystem. These effects are present in most materials, and serve to bring the system to a steady state under photoexcitation. The model employed in the present study is a one-band electronic model coupled to a single-mode Einstein phonon with a local Coulomb interaction. We solve the model in the Hartree-Fock approximation. This model is similar to the Peierls-Hubbard model on the mean-field level with an additional Holstein-type el-ph coupling term.

A. Ferroelectric ground state

We calculate the ground state phase diagram of the model, defined in Eq. (1), at half filling (one electron per BO_6 site) as a function of the model parameters (g, δ), with the phononic (Q) and electronic (ψ) degrees of freedom allowed to relax to their lowest energy configuration. Finite Q_j modes act as an onsite potential $\Delta_j^B = gQ_j$ for electrons. For $U = 0$, the ground state exhibits an insulating phase with a charge density wave (CDW) for $g > g_c$. The CDW is accompanied by lattice distortions reflected in finite Q_j modes. An increase in the onsite U drives the system toward the spin density wave (SDW). This is in agreement with previous theoretical studies of the two-site Hubbard-Holstein model [25].

In the present work, we focus on the CDW insulating phase. Figure 1(b) shows the magnitude of Q_i in the g-δ plane. The ground states obtained with $\delta \neq 0$ and $\Delta_i^B \neq 0$ lack inversion symmetry and are ferroelectric—these are equivalent to the Rice-Mele 1D-ferroelectric model that is often used to study the effects of BPVE [26]. The real-time study with $U \neq 0$ is a time-dependent version of the interacting Rice-Mele model. As we focus on the role of the el-ph interaction g_{br} in BPVE, we keep $U/t_{\rm hop} = 1$ constant throughout our study, so that the system is always in the CDW insulating phase.

The ferroelectric phase favors the formation of polarons. The binding energy of the polaron E_b is equal to the energy difference between the distorted case $Q_i \neq 0$ and the undistorted case $Q_i = 0$. Figure 1(b) shows the variation of E_b in the g_{br}-δ plane. The typical polaron binding energies measured in hole-doped transition-metal oxides are in the range of 100–500 meV [27]. In our current 1D model, the range of parameters $g_{br} = 2.50-3.50$ eV/Å and $\delta = 0 - 0.05$ eV reproduces a similar E_b.

III. PHOTOCURRENT GENERATION AND ITS EVOLUTION

To simulate the real-time dynamics of photocurrent generation and its evolution under a light field, we employ Ehrenfest dynamics. The one-particle electron wavefunctions evolve under the time-dependent Schrodinger equation, while the atoms obey the classical equations of motion. This framework can be considered similar to an implementation of real-time time-dependent density functional theory (rt-TDDFT) in the adiabatic approximation for the specified model Hamiltonian [28].

The effect of the linearly polarized light field, defined by the vector field $\vec{A}(t) = (A_o e^{\iota\omega_o t} + A_o e^{-\iota\omega_o t})\vec{e}_z$, where A_o is the amplitude of the vector potential and $\hbar\omega_o$ is the photon energy, is incorporated into the model Eq. (1) using the Peierls substitution method [29].

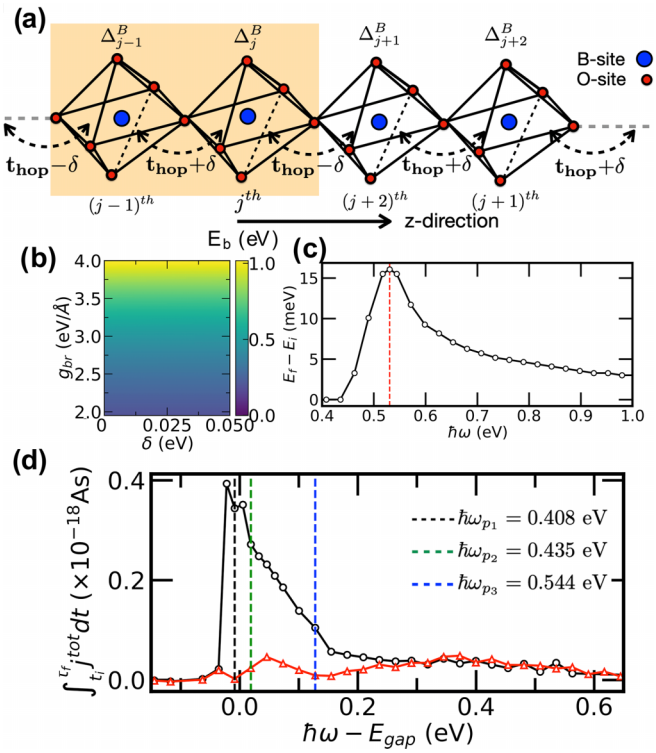

FIG. 1. (a) One dimensional chain of corner-connected BO_6-octahedra where B-type cations (blue circles) and O-type anions (red circles) occupy the center and corner of octahedra. The unit cell is shown in yellow; (b) Polaron binding energy $E_b = (E_{\rm pot} - E^{|Q=0|}_{\rm pot})$, within $g - \delta$. (c) Photon absorption density as a function of excitation energy. (d) Integrated current $\int j^{\rm tot}(t)dt$ as a function of excitation energy. The lines in black and red show $\int j^{\rm tot}(t)dt$ in the presence and absence of atom dynamics, respectively. (b), (c), and (d) consider $t_{\rm hop} = 0.50$ eV, $U = 0.50$ eV, K=10 eV/Å^2. (c) and (d) considers $\delta = 0.025$ eV and g_{br}=2.80 eV/Å. (d) uses $I = 3.14 \times 10^4$ W/cm^2 (i.e., $A_o = 0.001\ \hbar/ea_o$).

For the real-time simulations of the BPVE, we consider the polaronic ferroelectric state as the initial state with band gap $E_{\rm gap}$=0.411 eV at time t=0. In the initial state, the chain is dimerized with a staggered pattern of local distortion Q_i, and with zero initial velocities. The BPVE effect is investigated in the parameter ranges $\delta = 0.0 - 0.025$ eV and g_{br}=2.75 − 3.0 eV/Å while keeping $t_{\rm hop} = 0.50$ eV and $U = 0.50$ eV fixed.

The simulations are carried out with a time step dt=0.96 × 10^{-17} s in a supercell with 4 B-type sites and periodic boundary conditions. We used a N_k=800 point k-grid symmetric around the Γ point.

A. Spectral distribution of photocurrent

Firstly, we investigate the spectral distribution of the photon absorption density $D_p = \delta E_{f-i}/\hbar\omega$, where δE_{f-i} is a change in $E_{\rm tot} = E_{\rm kin} + E_{\rm pot}$, before and after a short 50 femtosecond Gaussian-shaped light pulse using A_o = 0.001 $\hbar/ea_o$. The system shows a broad absorption peak with a band gap of 0.411 eV, see Fig. 1(c).

Next, we consider the effect of a continuous-wave light field on the photocurrent. Figure 1(d) shows the spectrum of

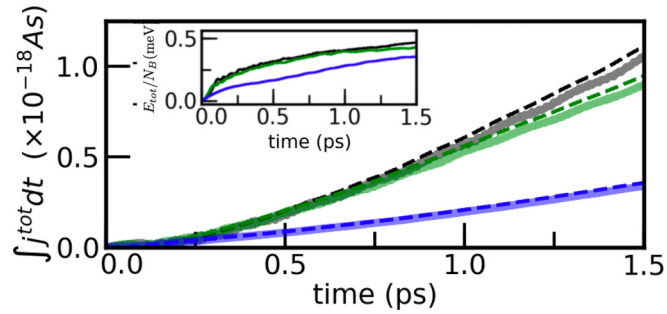

FIG. 2. (a) Evolution of total current $\int j^{\rm tot}(t, \omega_p)dt$ (dashed lines) and $\int j^{\rm scattering}(t)dt$ current component (faint-colored lines) at photon energy $\hbar\omega_{p_1} = 0.408$ eV (black), $\hbar\omega_{p_2} = 0.435$ eV (green), and $\hbar\omega_{p_3} = 0.544$ eV (blue), as indicated in Fig. 1(d). Inset shows the evolution of the total energy $E_{\rm tot} = E_{\rm kin} + E_{\rm pot}$.

the time integrated current $\int_{t_i}^{t_f} j^{\rm tot}(t)dt$, where the total current $j^{\rm tot}(t)$ is defined as

$$j^{\rm tot}(t) = \sum_n f_n \sum_{\sigma,j} e^{i\vec{A}(t)\bar{d}}(t_{\rm hop} + (-1)^j\delta) \times (\psi_{\sigma,j,n}(t)\psi^*_{\sigma,j+1,n}(t) - \psi_{\sigma,j+1,n}(t)\psi^*_{\sigma,j,n}(t))\vec{e}_z, \quad (2)$$

where we choose the interatomic distance $\bar{d}$ = 3.85 Å between B-type sites as the average distance between transition metal ions in correlated oxides [19,21]. The current is integrated over a period t_i=1.08 ps to t_f=1.45 ps. In the presence of atom dynamics, the system displays a strong photocurrent over a wide energy range between $\hbar\omega = 0.40 - 0.60$ eV. We attribute this photocurrent to ballistic current $j^{\rm ballistic}(t)$ generated as a result of asymmetric carrier scattering by phonon modes. In comparison, the photocurrent in the frozen-atom case is several times smaller. We attribute this contribution to the photocurrent to injection current induced by electron-hole (el-h) pair creation under linearly polarized light as discussed in Ref. [13].

B. Large phonon-assisted ballistic current

In Figs. 2 and 3, we show the evolution of the total photocurrent and carrier populations as a function of time at three different excitation frequencies $\hbar\omega_p$. In the beginning, the dynamics is highly nonequilibrium in nature, with a continuous increase in the photocurrent, excited-state populations, and total energy $E_{\rm tot} = E_{\rm pot} + E_{\rm kin}$ of the system, where $E_{\rm kin}$ is the kinetic energy of atoms. For excitation at ω_{p1}, the system reaches quasi-steady state at time $t \sim 1.0$ ps, which is reflected in the saturation of the photocurrent, excited state populations, and total energies. The time taken to reach steady state increases as the excitation frequency is increased to ω_{p2} and ω_{p3}. The correlation between the saturation of the photocurrent with the saturation of the carrier populations is consistent with the photocurrent being mostly ballistic current, which is sensitive to the carrier populations.

Optical excitations from the valence band to the conduction band in the polaronic ferroelectric state are accompanied by charge transfer between sites, altering local charge densities $\rho_i(t)$. The phonon modes $Q_i(t)$ are coupled with local change

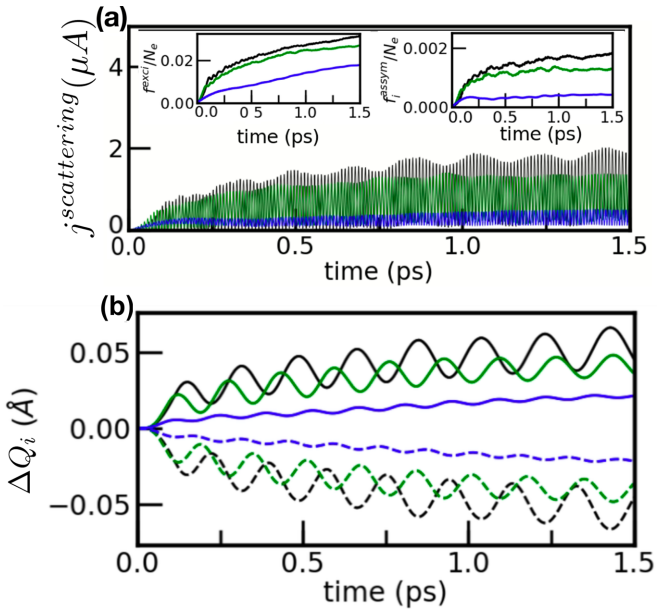

FIG. 3. (a) Evolution of instantaneous current $j^{\text{scattering}}(t)$. Left inset shows fraction of excited electrons. Right inset shows evolution asymmetric carrier momentum distribution $f^{\text{assym}} = \sum_{v,k}(\tilde{f}_{v,k} - \tilde{f}_{v,-k})$ of valence band. (b) dynamics of local phonon modes $\Delta Q_i = Q_i(t) - Q_i(t=0)$, where negative and positive $\Delta Q_i(t)$ corresponds to different B-type sites of the unit cell. For description of the colors, see Fig. 2.

densities $\rho_i(t)$. Thus, changes in $\rho_i(t)$ induce atomic displacements, which are primarily high-frequency optical phonon modes, as seen in Fig. 3(b).

Bulk photocurrents arise in the scattering picture [22] when carriers occupy an asymmetric carrier-momentum distribution $\tilde{f}_{m,k} \neq \tilde{f}_{m,-k}$ in the Brillouin zone. This asymmetric carrier momentum distribution can be induced by scattering from phonons or el-h pairs. Thus, the sum $j^{\text{scattering}}(t)$ of the ballistic and injection currents induced by el-ph and el-hole scattering is

$$\begin{aligned} j^{\text{scattering}}(t) &= j^{\text{ballistic}}(t) + j^{\text{inj}}(t) \\ &= -e\sum_{k,m} \tilde{f}_m(k,t) v_m(k,t), \end{aligned} \tag{3}$$

where $\tilde{f}_m(k,t)$ and $v_m(k,t)$ are the momentum distribution and the electron velocity in band m, respectively. For the present two-band model, the electron velocities $v_m(k,t)$ in band m are $v_m(k,t) = \partial_k \epsilon_m(k,t)$. We compute $v_m(k,t)$ using a finite difference method

$$v_m(k,t) = \frac{\epsilon_m(k+\delta k,t) - \epsilon_{m,t}(k-\delta k,t)}{2\delta k}. \tag{4}$$

The occupancy $\tilde{f}_m(k,t)$ of the eigenstates $\phi_m^{BO}(k,t)\rangle$ of the instantaneous electronic Hamiltonian is calculated by projecting the occupied one-particle wavefunctions $|\psi_n(k,t)\rangle$ on these eigenstates.

In general, asymmetric velocities $v_{m,k} \neq v_{m,-k}$ or by asymmetric occupations $\tilde{f}_{m,k} \neq \tilde{f}_{m,-k}$ can both give rise to bulk photocurrents, see Eq. (4). In this model, the generation of ballistic and injection currents is entirely due to asymmetric occupations because time-reversal symmetry of the model forbids asymmetric band velocities.

On comparing the computed scattering current $j^{\text{scattering}}(t)$ with the total current $j^{\text{tot}}(t)$ [Fig. 2(a)], we find that most of the photocurrent in this system can be explained by the scattering current. The remainder, which arises from carrier coherences instead of carrier populations [8], is understood to be the shift current. In this one-dimensional polaronic ferroelectric insulator, electronic transitions from the valence band to the conduction band are accompanied by a shift in the charge center which constitutes the shift current $j^{sh}(t)$. We find that the shift current $j^{sh}(t) = j^{\text{tot}}(t) - j^{\text{scattering}}(t)$; contribution remains very small in the presence and absence of atom dynamics.

Figure 3(a) shows the evolution of the instantaneous current $j^{\text{scattering}}(t)$, defined in Eq. (3), for different values of $\hbar\omega_p$. The evolution of the asymmetric carrier momentum distribution $\sum_{v,k}(\tilde{f}_{v,k} - \tilde{f}_{v,-k})$ in the valence band is shown in Fig. 3(a), right inset. Like the total current calculated from Eq. (2), asymmetric carrier momentum distribution also becomes almost constant for $t > 0.75$ ps, showing that a constant asymmetric carrier scattering rate is achieved in steady state. Although the el-el interaction U is small enough that el-ph scattering accounts for most of the photocurrent, el-el scattering plays a role in bringing the system to a steady state by acting as a relaxation process that limits asymmetric carrier distributions.

To investigate at the contribution of the injection current $j^{\text{inj}}(t)$ in $j^{\text{scattering}}(t)$, we repeat the simulations keeping the atoms frozen. In this case, $j^{\text{scattering}}(t)$ is purely the injection current, which is significantly lower compared to $j^{\text{scattering}}$ in the presence of atom dynamics, see the Supplemental Material [30] (see also Refs. [22,31] therein), showing a negligible contribution of the injection current.

C. Current versus intensity behavior

The strength of these relaxation processes in comparison to the light intensity $I = 1/2|A_o^2|\omega_o^2 c\epsilon_o$ is an important parameter that controls the behavior of bulk photocurrents. Figure 4(a) shows the behavior of the total current with intensity in the presence of atom dynamics. We observe a crossover from a linear current dependence on intensity to a deviation from linear behavior at higher intensities. The low-intensity limit is consistent with the predictions of perturbation theory [22]. A crossover to the high intensity limit was also obtained for injection currents under circularly polarized light using the Keldysh-Floquet formalism [17], where it was predicted that the current scales as the square root of intensity in the high intensity (slow relaxation) limit, not given by any order of perturbation theory. Our numerical simulations suggest that the Keldysh-Floquet analytical results derived for injection currents under circularly polarized light are likely to apply to other bulk photocurrents such as the phonon-induced ballistic photocurrent.

D. Effect of el-ph coupling and bond asymmetry

The magnitude of the phonon-induced ballistic current strongly depends on the form of el-ph coupling. In the present

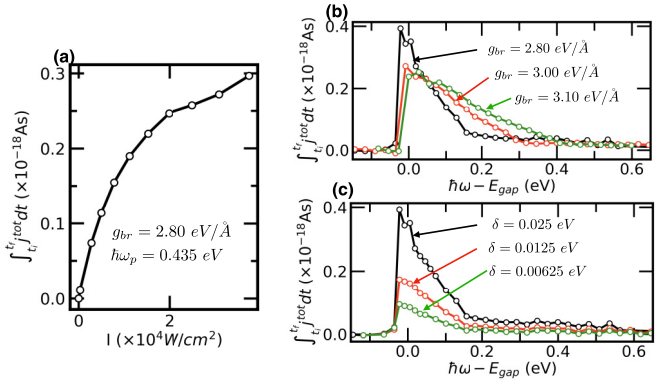

FIG. 4. (a) Integrated current $\int j^{\rm tot}(t)dt$ as a function of excitation intensity showing a sublinear behavior. (b) $\int j^{\rm tot}(t)dt$ for different values of el-ph coupling strength g_{br}; (c) $\int j^{\rm tot}(t)dt$ for different values of δ. Figure (a) uses $g_{br} = 2.80$ eV/Å and $\delta = 0.05$ eV. Figure (b) uses $I = 5.0$ mW (i.e., $A_o = 0.001\ \hbar/ea_o$) and $\delta = 0.025$ eV. Figure (c) uses $I = 3.14 \times 10^4$ W/cm^2 (i.e., $A_o = 0.001\ \hbar/ea_o$) and $g_{br} = 2.80$ eV/Å.

model, the Holstein-type el-ph coupling, where the electron density strongly coupled to the phonon modes [$\rho_j Q_j$, Eq. (1)], is responsible for creating a strong asymmetric carrier distribution. Polaronic materials, which include many ferroelectric materials, are likely to have an el-ph coupling containing a term of this form. It is expected that the Peierls-type el-ph coupling in ferroelectrics with high frequency phonon modes and high polaron binding energy will produce a similar large ballistic current response.

Now we look at the effect of the el-ph coupling parameter g_{br} and the hopping asymmetry δ on the current. Figure 4(b) shows the total current $\int j^{\rm tot}(t)dt$ for four different el-ph coupling strengths. Even though some amount of el-ph coupling is necessary to create an asymmetric carrier distribution, a larger value of el-ph coupling does not always result in larger ballistic current. For this range of parameters, we observe that $\int j^{\rm tot}(t)dt$ decreases with increasing g_{br} close to the band edge, but has the opposite trend away from the band edge. This is because besides asymmetric carrier scattering rate, the carrier velocities have a significant impact on the ballistic current [Eq. (3)]. The renormalization of carrier velocities near the band edge is reflected in the higher band edge $\int j^{\rm tot}(t)dt$ at $g_{br} = 2.80$ eV/Å, compared to $g_{br} = 3.00$ eV/Å and 3.10 eV/Å.

The model parameter δ, see Eq. (1), describes the relative asymmetry between the bonds. A higher value of δ means greater asymmetry between the bonds. Changing δ from 0.00625 eV to 0.0125 and 0.025 eV [Fig. 4(c)] enhances the current almost by a factor of two and four, respectively. This shows that a higher δ generates a stronger BPVE. This is similar to the behavior of the shift current, which also increases with δ.

E. Material design for BPVE

Our present study highlights the importance of optical phonon modes and the polaronic effect in inducing a strong photocurrent in ferroelectric insulators. We show that el-ph coupling to optical phonon modes produces strong zero-frequency ballistic current. Multiferroic oxides and charge-transfer organic salts are potential candidates for the realization of strong BPVE. In multiferroic oxides, ferroelectricity originates from the underlying charge and orbital order that are strongly coupled to local atomic distortions, and the band gap is sensitive to these distortions [19–21,32]. The d-d-type electronic transitions across the band gap in such systems are expected to generate a strong nonlinear photovoltaic response.

IV. SUMMARY

Using a tight-binding model with realistic parameters, we have shown that phonon-induced ballistic current can be supported in a polaronic ferroelectrics, and it can be the dominant contributor to the bulk photocurrent when the right form of el-ph coupling is present. The high-frequency phonon modes that are coupled to electronic excitations generate an asymmetric momentum distribution of charge carriers and induce a strong directional ballistic photocurrent. Our study suggests that the effects of optical phonon modes strongly influence the BPVE properties, and understanding the contribution of these effects is essential to boost the bulk photovoltaic response in ferroelectrics known to exhibit polaronic character.

ACKNOWLEDGMENTS

S.R., T.O., and L.Z.T were supported by the Computational Materials Sciences Program funded by the US Department of Energy, Office of Science, Basic Energy Sciences, Materials Sciences and Engineering Division. Additional support for absorption calculations was obtained from the Molecular Foundry, a DOE Office of Science User Facility supported by the Office of Science of the U.S. Department of Energy under Contract No. DE-AC02-05CH11231.

[1] N. Bloembergen, *Nonlinear Optics*, 4th ed. (WORLD SCIENTIFIC, 1996), https://www.worldscientific.com/doi/pdf/10.1142/3046.
[2] R. Boyd, *Nonlinear Optics*, 4th ed. (Academic Press, 2020).
[3] R. von Baltz and W. Kraut, Phys. Rev. B **23**, 5590 (1981).
[4] V. I. Belinicher and B. I. Sturman, Soviet Physics Uspekhi **23**, 199 (1980).
[5] W. Kraut and R. von Baltz, Phys. Rev. B **19**, 1548 (1979).
[6] B. I. Sturman and V. M. Fridkin, *The Photovoltaic and Photorefractive Effects in Noncentrosymmetric Materials* (Gordon and Breach Science Publishers, 1992).
[7] B. I. Sturman, Phys. Usp. **63**, 407 (2020).
[8] L. Z. Tan, F. Zheng, S. M. Young, F. Wang, S. Liu, and A. M. Rappe, npj Comput. Mater. **2**, 16026 (2016).
[9] V. I. Belinicher and B. I. Sturman, Sov. Phys. Solid State **20**, 476 (1978).

[10] V. I. Belinicher and B. I. Sturman, Ferroelectrics **83**, 29 (1988).
[11] A. M. Burger, R. Agarwal, A. Aprelev, E. Schruba, A. Gutierrez-Perez, V. M. Fridkin, and J. E. Spanier, Sci. Adv. **5**, eaau5588 (2019).
[12] V. V. Men'shenin, Phys. Solid State **45**, 2131 (2003).
[13] T. Kaneko, Z. Sun, Y. Murakami, D. Golež, and A. J. Millis, Phys. Rev. Lett. **127**, 127402 (2021).
[14] J. E. Sipe and A. I. Shkrebtii, Phys. Rev. B **61**, 5337 (2000).
[15] P. T. Mahon, R. A. Muniz, and J. E. Sipe, Phys. Rev. B **100**, 075203 (2019).
[16] P. Král and J. E. Sipe, Phys. Rev. B **61**, 5381 (2000).
[17] O. Matsyshyn, F. Piazza, R. Moessner, and I. Sodemann, Phys. Rev. Lett. **127**, 126604 (2021).
[18] T. Barik and J. D. Sau, Phys. Rev. B **101**, 045201 (2020).
[19] S. Rajpurohit, C. D. Pemmaraju, T. Ogitsu, and L. Z. Tan, Phys. Rev. B **105**, 094307 (2022).
[20] S. Rajpurohit, C. Jooss, and P. E. Blöchl, Phys. Rev. B **102**, 014302 (2020).
[21] M. Sotoudeh, S. Rajpurohit, P. Blöchl, D. Mierwaldt, J. Norpoth, V. Roddatis, S. Mildner, B. Kressdorf, B. Ifland, and C. Jooss, Phys. Rev. B **95**, 235150 (2017).
[22] Z. Dai, A. M. Schankler, L. Gao, L. Z. Tan, and A. M. Rappe, Phys. Rev. Lett. **126**, 177403 (2021).
[23] M. Nakamura, S. Horiuchi, F. Kagawa, N. Ogawa, T. Kurumaji, Y. Tokura, and M. Kawasaki, Nat. Commun. **8**, 281 (2017).
[24] B. M. Fregoso, T. Morimoto, and J. E. Moore, Phys. Rev. B **96**, 075421 (2017).
[25] H. Fehske, A. P. Kampf, M. Sekania, and G. Wellein, Eur. Phys. J. B **31**, 11 (2003).
[26] M. J. Rice and E. J. Mele, Phys. Rev. Lett. **49**, 1455 (1982).
[27] S. Mildner, J. Hoffmann, P. E. Blöchl, S. Techert, and C. Jooss, Phys. Rev. B **92**, 035145 (2015).
[28] S. Rajpurohit, J. Simoni, and L. Z. Tan, Nanoscale Adv. **4**, 4997 (2022).
[29] R. Peierls, Z. Phys. **80**, 763 (1933).
[30] See Supplemental Material at http://link.aps.org/supplemental/10.1103/PhysRevB.108.104305 for the description of the real-time simulation methodology, the convergence results, and a comparison to perturbative studies, which also includes Refs. [22,31].
[31] C.-C. Lee, Y.-T. Lee, M. Fukuda, and T. Ozaki, Phys. Rev. B **98**, 115115 (2018).
[32] S. Rajpurohit, L. Z. Tan, C. Jooss, and P. E. Blöchl, Phys. Rev. B **102**, 174430 (2020).